Carbon 249 (2026) 121215

Contents lists available at ScienceDirect

Carbon

journal homepage: www.elsevier.com/locate/carbon

Writing, rewriting, and directing matter on a graphene canvas

Raul D. Rodriguez [a,*], Pavel Bakholdin [a], Tuan-Hoang Tran [a], Elizaveta Dogadina [a], Dmitry Cheshev [a], Dmitry Kogolev [a], Maxim Fatkullin [a], Jin-Ju Chen [b], Tian Ma [c], Shuang Li [c], Chong Cheng [c], Evgeniya Sheremet [a]

[a] Tomsk Polytechnic University, Lenin ave. 30, Tomsk, 634050, Russia
[b] School of Materials and Energy, University of Electronic Science and Technology of China, Chengdu, 610054, China
[c] College of Polymer Science and Engineering, State Key Laboratory of Advanced Polymer Materials, Sichuan University, Chengdu, 610065, China

ARTICLE INFO

Keywords:
All-carbon electronics
Graphene oxide
Graphene transistor
Electrochemical lithography

ABSTRACT

Conventional fabrication of integrated carbon electronics often requires material deposition or transfer, which inevitably leads to surface contamination and structural defects. Here, we present a monolithic "Write-Rewrite-Direct" approach for in situ sequential programming of carbon's optical, electrical, and chemical properties from a single parent graphite crystal, overcoming the challenges of material transfer. First, we introduce Catalyst-Enhanced Electrochemical Lithography (CEEL), an acid-free route that exploits MoS_2 electrocatalysis to "write" atomically smooth epitaxy-like graphene oxide (GO) directly onto graphite. In contrast to conventional electrochemical oxidation of graphite, which yields rough surfaces, CEEL produces mechanically robust, vivid photonic structures with intense structural colors. We validate this monolithic integration by fabricating the first all-carbon field-effect transistor with a vertical gate-dielectric-channel configuration, without any lithographic patterning of contacts or lift-off processes. Second, we "rewrite" these films with a tightly focused laser to produce laser-reduced graphene oxide (LrGO) vertical interconnects. This enables us to draw all-carbon free-form, high-resolution LrGO circuits within the larger, electrochemically defined GO structure. Finally, we exploit this hierarchical control to "direct" the selective assembly of plasmonic nanostructures onto the LrGO patterns, integrating plasmonic microreactors and chemical sensing capabilities. This "Write-Rewrite-Direct" paradigm is a potential enabler of next-generation all-carbon electronics, offering a maskless route to creating dynamic, reconfigurable surfaces, including field-effect transistors and advanced sensing and photocatalytic platforms monolithically integrated in a single device.

1. Introduction

Current technology relies heavily on our ability to control and exploit surface properties, enabling applications from microelectronics to smart implants [1,2]. However, a persistent challenge and fundamental fabrication bottleneck in all-carbon electronics is the need for material transfer and deposition. Although traditional photolithography provides high spatial accuracy, it is a rigid, multi-step process that requires complex and costly infrastructure. Therefore, a major goal in engineering surface properties is developing a strategy that enables simple, sequential programming of optical, electronic, and chemical functionalities on a surface using readily available tools. Maskless methods, such as laser processing, can induce surface modifications, including ablation, composite formation, and surface texturing [3–5]. Environmental patterning methods using laser [6,7] or plasma [8] reduction can change surface properties depending on the atmosphere; however, these changes are irreversible. Meanwhile, electrochemistry (EC) enables reversible control of surface properties through redox reactions by adjusting the applied potential [9–12]. Surface properties can also be tuned through chemical functionalization. For instance, electronic properties, such as n-type or p-type doping of graphene, can be achieved by functionalizing graphene with poly(ethylene imine) or diazonium salts, respectively [13]. Furthermore, EC treatment with diazonium salts can simultaneously exfoliate and functionalize graphene, yielding materials suitable for flexible and implantable electronics [14–16]. While these approaches have been implemented at the micro- and nano-scale [17,18], a unified platform for monolithic device integration remains elusive.

* Corresponding author.
E-mail address: rodriguez@tpu.ru (R.D. Rodriguez).

https://doi.org/10.1016/j.carbon.2025.121215
Received 2 October 2025; Received in revised form 19 December 2025; Accepted 27 December 2025
Available online 29 December 2025

Although electrochemical [19–21] and laser patterning [22–24] techniques have been explored previously, existing methods face a fundamental bottleneck: electrochemical processes often produce rough, delaminated films, while laser reduction involves additional steps, such as transferring the original graphene oxide (GO) material onto substrates before processing, leading to interface contamination, wrinkles, and structural inhomogeneity. In this work, we address these issues by presenting a new monolithic approach that enables the fabrication of all-carbon functional devices in situ from a single parent graphite substrate.

First, we introduce catalyst-enhanced electrochemical lithography (CEEL) to 'write' atomically smooth, epitaxy-like, GO thin films with vibrant colors directly onto graphite. Unlike standard EC oxidation, which often yields defective, small, delaminated flakes due to aggressive oxygen-evolution reactions (OER), CEEL employs MoS_2 to catalyze the generation of reactive oxygen species (ROS) for graphite oxidation. It ensures long-term stability through SO_4^{2-} ion intercalation without requiring strong acids and reduces gas formation by controlling OER. This enables the creation of large-scale, mechanically robust GO films with a surface roughness <2.5 nm. These GO films, formed directly on graphite, demonstrate exceptional mechanical durability compared to transferred exfoliated GO and display vivid colors not previously reported for other EC-produced GO. In the case of CEEL-generated GO, these photonic structures are not periodic dielectric configurations like photonic crystals, but rather patterns with structural colors from thin-film interference. Such structural colors are valuable for their stability and potential in photonics applications, from lasers to sensors [25]. We demonstrate the technological potential and robustness of this stack by fabricating the first monolithic all-carbon field-effect transistor (FET) with a vertical gate-dielectric-channel configuration. The impact of this development lies in the realization of a FET device without any lithographic patterning of contacts or lift-off processes, exploiting the intrinsic vertical gradient of the CEEL film.

Second, we "Rewrite" these structures by laser processing to selectively reduce GO with micrometer precision, enabling the creation of high-resolution vertical interconnects and planar free-form circuits on the planar laser-reduced GO (LrGO).

Third, we exploit engineered electrical and chemical patterns to "Direct" the selective growth of gold- and silver-based plasmonic nanoreactors capable of in situ induction and detection of chemical reactions via surface-enhanced Raman spectroscopy (SERS), thereby enabling the direct hierarchical integration of chemical sensing with carbon electronics.

This work presents a straightforward approach that overcomes the limitations of transfer-based lithography to create complex, reconfigurable surfaces that impact all-carbon optoelectronics and sensing platforms.

2. Experimental section

2.1. Materials

Highly oriented pyrolytic graphite (HOPG) flakes are peeled off with adhesive tape from HOPG ZYA 0.4 ± 0.1° (Kapella, Russia) and fixed onto glass (15 × 25 mm^2) using double-sided tape.

10 mg of MoS_2 powder (GC "SMM", LLC, Russia), with physicochemical characteristics summarized in Fig. S1, was dispersed in 1.5 mL of ethanol (95 %, Svetoform, Russia). The resulting dispersion was diluted with 15 mL of distilled water. To prevent agglomeration, the MoS_2 dispersion was sonicated for 5 min before each experiment.

A gold-coated insulated copper wire (diameter: 180 μm) served as the counter electrode. Gold nanoparticles were electrodeposited onto the copper wire via electrochemical reduction in 2 μL of 1 mM $HAuCl_4$ for 30 s at a constant potential of −2.5 V using an APS605H DC power supply (Wanptek, China) with HOPG as the anode. The distance between the copper wire and the HOPG surface was maintained at 0.75 μm throughout the deposition.

4-nitrobenzenethiol (4-NBT), technical grade 80 % (Sigma-Aldrich, Germany), was used as a model in the photocatalysis experiment.

2.2. CEEL and laser processing

Electrochemical lithography was performed in a MoS_2 dispersion using an electrochemical cell (Shanghai Yuce Electronic Technology, China) with a potentiostat-galvanostat P-45X (Electrochemical Instruments, Russia). HOPG, an Au-coated copper wire, and Ag/AgCl electrode were used as working, counter, and reference electrodes, respectively. The HOPG electrode was immobilized at the bottom of the cell, while the counter electrode was positioned perpendicularly above it, and the reference electrode was inserted through a side port. The distance between the HOPG and the copper wire was set to either 0.75 μm or 1.5 μm to produce patterns with lateral dimensions of 0.7 mm and 1.0 mm, respectively. Electrical signals of various shapes and polarities, with specified parameters, were applied using a potentiostat-galvanostat (details are provided in the Supporting Information). After electrochemical lithography, the sample was rinsed with distilled water and dried using compressed air.

Laser reduction of GO was performed using a 532 nm continuous-wave diode laser (Matchbox, Integrated Optics, Lithuania), equipped with a 100x objective. The laser beam diameter after the 100x objective was approximately 800 nm. Laser power was optimized over the range 0.1–5 mW to achieve optimal LrGO. Scanning speed was fixed at 20 μm/s.

Electrochemical deposition of metals on LrGO: Metal nanoparticles were deposited on LrGO by the electrochemical method. In brief, metal nanoparticles were deposited in a two-electrode configuration, with LrGO and a 50 μm-diameter gold wire employed as cathode and anode, respectively. Ag deposition was performed from an aqueous $AgNO_3$ solution (0.1 M) at a constant potential of −1 V for 30 s. Au deposition was performed in an aqueous solution of 0.1 mM $HAuCl_4$ at −1.5 V for 30s.

2.3. Characterization

Atomic force microscopy (AFM): The topography and thickness of the GO film were investigated using an NTEGRA PRIMA atomic force microscope (NT-MDT, Russia) with NSG10 tips (NT-MDT, Russia). The NSG10/Pt (NT-MDT, Russia) tips were used to study surface potential (SP) in Kelvin probe force microscopy. The I–V curves were obtained in current-sensing atomic force microscopy using NSG10/Pt tips (NT-MDT, Russia).

Raman spectroscopy: Optical images, Raman, and photoluminescence spectra were recorded using a Raman spectrometer (NT-MDT SI, Russia), equipped with 10x, 20x, and 100x objectives (Mitutoyo, USA) and 457, 532, 633, 785 nm continuous-wave diode lasers Matchbox (Integrated Optics, Lithuania).

X-ray photoelectron spectroscopy (XPS): A Thermo Fisher Scientific NEXSA spectrometer (Thermo Fisher Scientific, USA) with a monochromated Al Kα X-ray source (1486.6 eV) was used. Survey spectra were recorded with 200 eV radiation and an energy resolution of 1 eV. For the high-resolution spectra, the pass energy was 50 eV, and the energy resolution was equal to 0.1 eV. The spot area was 400 μm^2. The flood gun was used for the charge compensation. The XPS spectra were analyzed using Avantage software.

Scanning electron microscopy (SEM): SEM images and energy-dispersive X-ray (EDX) spectra were acquired using a Thermo Fisher Scientific Apreo 2 S LoVac (Thermo Fisher Scientific, USA).

Transistor characterization: Transistors were fabricated by placing two 50-μm-diameter gold wires in direct contact with the graphene oxide (GO) film, serving as the drain and source electrodes, with an interelectrode spacing of 200 μm. The underlying HOPG substrate functioned as the back-gate electrode. Current–voltage (I–V)

characteristics were acquired using an MFLI Lock-in Amplifier (Zurich Instruments, Germany). A DC gate voltage (V_{GS}) was applied on HOPG, while a small AC drain–source voltage (V_{DS}) at 514 Hz was superimposed; the resulting drain current (I_D) was measured at the same frequency (514 Hz) to effectively isolate the channel response from capacitive coupling through the gate.

Temperature measurement: To estimate the effect of temperature on the GO film, a GO CEEL sample was placed on a heater mounted on the atomic force microscope (NT-MDT, Russia). The intensity map of reflected radiation from a 532 nm laser in the selected area at different temperatures was recorded by the Raman spectrometer.

Photocatalysis experiment: To conduct the photocatalysis experiment, LrGO CEEL, with deposited Ag nanoparticles, was immersed in a 1 mM 4-NBT solution for 3 h in the dark. After that, the sample was rinsed with distilled water and ethanol. The photocatalytic conversion of 4-NBT to 4-4′-dimercaptoazobenzene (DMAB) was evaluated by Raman spectroscopy.

3. Results and discussion

First, we introduce the concept of CEEL, illustrated in Fig. 1A, which exploits an MoS_2 electrocatalyst and the localized electric field between HOPG and an Au-coated copper microelectrode. Initially, we expected that a microelectrode would provide a strong electric field gradient for the oxidation of graphite in ethanol and water, thereby bypassing the need for H_2SO_4, which has been widely used for decades for electrochemical oxidation and exfoliation of graphite [26]. However, we observed a rather uncontrolled reaction, characterized by the formation of large bubbles (see Supporting Video 1), which resulted in rough, grainy patterns (Fig. 1B). These patterns followed the edges and defects

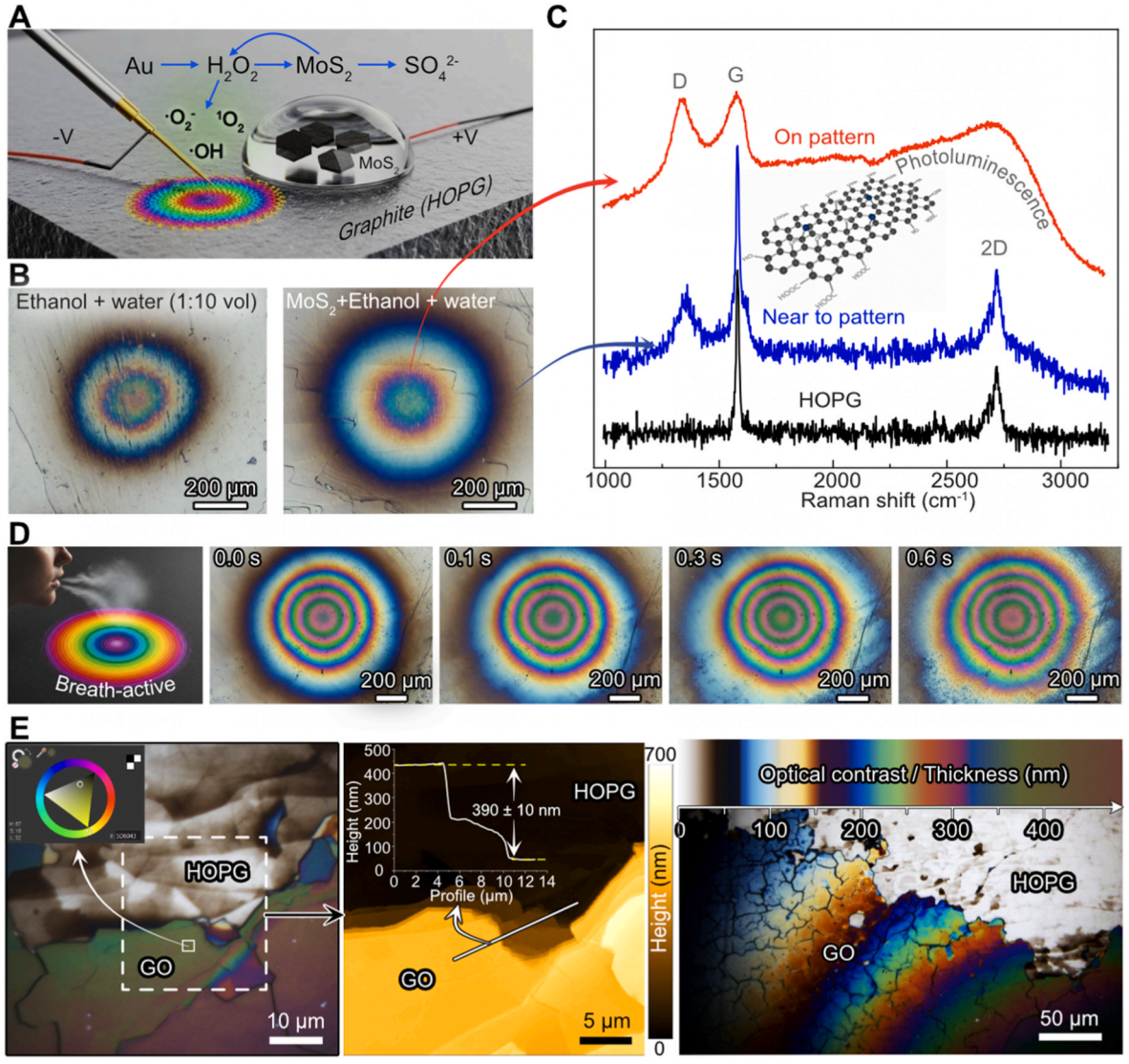

Fig. 1. (A) Schematic of the CEEL process. A localized electric field is applied between a gold-coated copper wire (counter electrode) and HOPG (working electrode). The gold-coated copper wire catalyzes the reduction of dissolved oxygen to produce hydrogen peroxide (H_2O_2). Dispersed MoS_2 flakes act as an electrocatalyst, activating H_2O_2 to ROS like •OH, $•O_2^-$, $^1O_2$ and oxidizing to form sulfate ions (SO_4^{2-}). These sulfates then intercalate between the graphene layers while the ROS uniformly oxidize the HOPG surface, resulting in the formation of a homogenous GO photonic pattern. (B) Optical micrographs comparing GO patterns formed with an ethanol/water electrolyte (left) and with the addition of a MoS_2 electrocatalyst (right), which produces a more uniform and intensely colored structure. (C) Raman spectra taken on the GO pattern, near the pattern, and on the pristine HOPG substrate. The emergence of the D peak and broadening of the G peak on the pattern confirm the formation of GO. (D) Time-lapse optical images showing the pattern change of the GO film upon exposure to breath, demonstrating its environmental-responsive nature. (E) Optical and AFM images of a GO film partially delaminated under harsh ultrasonication conditions. The AFM height profile allows the correlation between color and thickness, demonstrating that the colors arise from thin-film interference. (For interpretation of the references to color in this figure legend, the reader is referred to the Web version of this article.)

present on the HOPG surface, given their higher electrochemical activity compared to the basal plane, as shown by Gewirth and Bard [27]. It has been reported that Au-decorated Cu nanostructures catalyze the oxygen reduction reaction, generating H_2O_2 [28]. Since the electrode in our CEEL experiment is an electrically insulated copper microwire with only its cross-section exposed and coated with electrochemically deposited gold nanostructures, dissolved oxygen in the electrolyte is converted into hydrogen peroxide as described by equation (1). We hypothesized that incorporating MoS_2 would enable the generation of ROS from H_2O_2 [29]. The mechanism behind ROS generation involves the exfoliation of MoS_2 in the presence of H_2O_2, accompanied by the formation of a metallic-like, electron-rich 1T phase. These active sites catalyze the reduction of H_2O_2, facilitating the formation of hydroxyl radicals (•OH) as shown in equation (2), accompanied by the successive generation of superoxide and singlet oxygen radicals [29]. These ROS uniformly attack both basal planes and edges, facilitating a homogeneous conversion to graphene oxide [30]. To test this hypothesis, we conducted control experiments using MoS_2 multilayer powder ultrasonicated in an ethanol-water (1:10 vol) solution. Control experiments using different solutions (see Fig. S2) confirmed that MoS_2 plays a crucial role in reaction smoothness and control, as well as in reducing bubble size and the rate of their release (see Supporting Video 2). To elucidate the mechanism behind CEEL, we analyzed the thermodynamic and kinetic influence of MoS_2 on the oxidation process (Fig. S3 and S4). As shown in the galvanostatic pulses in Fig. S4F, the operating potential required to start driving the oxidation current is significantly lower (~1.5 V) in the presence of MoS_2 compared to the control electrolyte without the catalyst (>2.5 V). This high-voltage regime drives vigorous gas evolution ($2H_2O \rightarrow O_2$), physically disrupting the graphite surface and yielding the rough, defective morphology observed in the control samples (Fig. 1B). In contrast, the addition of MoS_2 opens a catalytic pathway that lowers the activation energy for ROS generation. This shifts the reaction selectivity away from the disruptive OER and toward the chemical functionalization of the carbon lattice. The suppression of gas bubbles (see Supporting Videos) and the formation of atomically smooth, epitaxy-like GO films (Fig. S11) serve as the physical signature of this non-disruptive, catalytically controlled oxidation. Furthermore, the time stability of the resulting films provides evidence for successful ion intercalation and covalent lattice integration. While GO patterns formed in simple water/ethanol electrolytes fade within days due to the desorption of intercalated physisorbed species (Fig. S6), the CEEL-generated films remain stable for months. This confirms that sulfate and oxide groups are not merely physisorbed but have participated in the permanent oxidation of the graphene layers, consistent with the high degree of functionalization observed in XPS (Fig. 3). This stable, expanded lattice remains hydrophilic, allowing for the reversible water intake observed during the breathing experiments (Fig. 1D and S10).

The impact of MoS_2 flakes dispersed in powder form and their electrochemical activity were investigated by Manyepedza et al. [31]. We also observed diffusion of large MoS_2 flakes in video recordings during our CEEL reactions (see Supporting Video 3).

$$O_2 + 2H^+ + 2e^- \rightarrow H_2O_2 \quad (1)$$

$$H_2O_2 + e^- \rightarrow \bullet OH + OH^- \quad (2)$$

$$MoS_2 + 9H_2O_2 \rightarrow MoO_4^{2-} + 2SO_4^{2-} + 6H^+ + 6H_2O \quad (3)$$

We confirmed the different reaction pathways using electrochemical methods. Cyclic voltammograms (CV) recorded in electrolytes without MoS_2 showed oxidation peaks at approximately 0.5 V (Fig. S4A), indicating the formation of carbonyl groups [32], followed by a rapid, uncontrolled onset of OER at approximately 1.8 V (Fig. S4B). In contrast, adding MoS_2 resulted in suppressed oxidation peaks and an shift in the OER, demonstrating modulation of the reaction (Fig. S4C–D). The suppression of these parasitic reactions is key to the controlled layer-by-layer oxidation that defines CEEL.

The superior control offered by CEEL enabled us to design patterns with distinct characteristics. For instance, by adjusting the number of applied current cycles, we can control the film thickness, color, number of rings, and lateral size of the GO pattern (see Fig. S5). The higher number of applied current cycles, the larger lateral size of the GO pattern, which can reach more than a millimeter, an unprecedented size of monolithic GO film compared to the recorded average size of GO of 188.3 μm [33,34]. By including negative potentials during cycling (−100 to +400 μA), we were able to drastically improve the time stability of the photonic structures, from fading noticeably after only 5 days to showing vibrant colors without signs of degradation for up to 6 weeks (see Fig. S6). We attribute this enhanced stability to the increased layer expansion, which pushes the negatively charged SO_4^{2-} ions intercalated between the layers [30]. In the absence of MoS_2, intercalation and layer expansion were less efficient, resulting in color fading over time.

This summary explains the mechanism of HOPG oxidation and highlights the major structural differences between those formed with and without MoS_2. Initially, we focus on oxidation in the absence of MoS_2. Electrochemical experiments showed an oxidation peak associated with the formation of C═O functional groups, primarily at defect edges, which are typical of mono- and multi-atomic steps in HOPG. When the OER begins, polar solvent molecules move significantly near the carbon electrode, interacting with these oxygen-rich groups. This interaction causes the HOPG surface to crack, forming rough, uneven photonic structures that render the pre-existing defects in HOPG more evident (see Fig. 1B). When MoS_2 is added, an intermediate reaction occurs, producing ROS and SO_4^{2-} ions via interactions between H_2O_2 and MoS_2. The ROS then reacts with HOPG in a non-specific, uniform manner, spreading oxygen functionalities evenly across the surface and suppressing cracking. Meanwhile, a positive potential drives SO_4^{2-} ions into the interlayer space, stabilizing the photonic structures. Although ROS formation might be expected to persist after potential removal, in this case, ROS generation is driven by electrocatalytic H_2O_2 production, which ceases when the potential is turned off. Additionally, persistent radicals in the solution are quenched by the ethanol in the electrolyte. These conditions guarantee that the reaction is controlled by the applied potential, limiting the influence of self-sustaining and self-propagating radicals.

Chemical imaging with Raman microscopy in Fig. S7 confirms that these photonic structures arise from oxidation of the graphite substrate, resulting in the formation of GO films, as evidenced by the broad D and G peaks of comparable intensity. Representative Raman spectra in Fig. 1C show the evolution of the carbon features. The control Raman spectrum from pristine HOPG exhibits a sharp G band with a full width at half maximum (FWHM) of 14.1 ± 0.7 cm^{-1}. In contrast, the GO pattern and its surroundings exhibit a broad G peak with an FWHM of 110 ± 10 cm^{-1}. The most representative Raman feature of GO is the D peak at approximately 1350 cm^{-1}, which is activated by defects in the carbon lattice introduced by oxygen-containing groups and other structural defects. This D peak is absent in the Raman spectrum of HOPG (Fig. 1C) because of the high crystallinity of the pristine material. Due to the low thickness of the GO film, particularly at the thinner GO regions at the pattern periphery, and GO's optical transparency, contributions from the underlying HOPG substrate will inevitably be visible in the Raman spectra recorded at the thinnest regions of the GO pattern, as deduced from the transmittance data in the inset in Fig. S7. In addition to the D band on the pattern, there is a strong, broad band at higher wavenumbers due to luminescence [22]. This broadband photoluminescence (PL) exhibits the behavior reported earlier for thin GO films, where the PL peak shifts with the excitation wavelength (see Fig. S8). Such PL emission is attributed to transitions from the bottom of the conduction band and neighboring localized states to the wide valence band, in which labile oxygen-containing groups are involved [35,36].

We found that these colorful radial patterns were highly sensitive to environmental conditions, including temperature changes (see Fig. S9

and Supporting Video 4) and airflow induced by breathing on them (Fig. 1D and Fig. S10). We observed that, with increasing temperature, the rings in the GO CEEL pattern shift toward the center (see Fig. S9), which we attribute to a decrease in film thickness due to water evaporation from the interlayer space, thereby reducing the distance between the GO sheets [37]. The pattern's response to breathing is illustrated in Fig. 1D, which shows its evolution over a 1-s period from expansion to recovery to its initial state (Fig. S10). We attribute the changes in the pattern during breathing to water condensation, which alters the conditions for interference and thus the pattern's color. In addition to changes at the periphery of the pattern over time, the center shifts from a growing green circle with an emerging pink center to an overgrown green ring. The situation then repeats periodically (the pink center returns to green), consistent with thin-film interference. We observe in real time the dynamics of condensation of a water film enabled by this patterned GO structure, as shown in Supporting Video 5. One straightforward way to exploit this effect in high-impact applications is to functionalize the GO CEEL surface with a ligand, receptor, or antibody that selectively binds a disease biomarker, such as COVID-19 [38] or *Helicobacter pylori* [39]. This targeted color change is similar to surface plasmon resonance (SPR) sensors but does not require gold or other complex coatings; it paves the way for the future design of non-plasmonic all-carbon optical sensors. More generally, this approach could be helpful for diagnostic purposes, particularly for addressing respiratory diseases, which are among the leading causes of death worldwide. In biomedical applications, GO-based ionic transistors have attracted considerable attention due to their flexibility when combined with polyelectrolytes, thereby forming a sensing platform for virus detection [40,41]. Given the sub-second response of the pattern to breathing, this could enable the development of responsive smart surfaces for rapid detection of molecular markers, thereby facilitating the early diagnosis of chronic obstructive pulmonary disease, which accounts for over 3 million deaths worldwide, according to the World Health Organization [42].

So far, GO-based structural colors have only been fabricated from exfoliated GO sheets [25,43], which are mechanically unstable and poorly adhere to substrates, leading to delamination. One notable characteristic of our GO films, in contrast to conventional GO layers obtained by the Hummers' method [44,45], is that they are monolithically grown on a crystalline carbon substrate via an epitaxial-like growth process (Fig. S11), resulting in impressive robustness. We verified the structural robustness of the GO patterns by subjecting the samples to harsh mechanical conditions in an ultrasound bath cleaner. For comparison, we also subjected GO films obtained by Hummers' method (Graphenea, Spain) to the same conditions (see Fig. S12A and S12B in the Supporting Information). While the GO films obtained from dispersions readily disappeared from the HOPG substrate, the monolithic GO films remained largely unaffected, demonstrating the unprecedented robustness of these structures and implications for GO safety, as they minimize environmental release, a major persistent issue in GO applications [46].

The ultrasonication experiments enabled us to elucidate the mechanism behind these structural colors. Under the harshest ultrasonication conditions (1 min), some GO layers peeled off, allowing us to measure the thickness of the remaining layers and correlate thickness with color, as shown in Fig. 1E (for more details, see Fig. S13). AFM topography and optical images of GO CEEL on HOPG are presented in Fig. 1E and Fig. S13. The GO thickness was estimated based on the relative height to HOPG; this measurement carries an uncertainty of up to ~10 nm due to residual ultrathin GO layers that remained after sonication (see Fig. S13A-B). Subsequently, the color of GO CEEL was determined using the color picker tools in Affinity Designer, enabling precise identification. As illustrated in Fig. 1E, the relationship between color and film thickness reveals a clear trend: moving radially outward from the center, the GO thickness decreases, and the observed color exhibits periodic shifts - consistent with optical interference effects from a thin-film stack. In the outermost regions, where the film is thinnest (typically <10 nm, see Fig. S13C), the structure appears light gray, reflecting the low optical absorption of such ultrathin layers. In our experiments, the GO thickness spans from near-zero up to ~500 nm. Notably, the maximum achievable thickness and consequently the number of interference rings are governed by the oxidation extent, which can be tuned by varying the number of CEEL cycles (see Fig. S5).

There has been some debate in the literature about the origin of such colorful patterns in GO, with the mechanism attributed to either photonic crystal formation or thin-film interference. The AFM results in Fig. 1E provide evidence of a correlation between GO color and thickness, confirming the thin-film interference mechanism [25,47].

The Raman and AFM results showed that CEEL produced a GO film on the electrically conductive carbon substrate (HOPG), suggesting that this configuration could be used as an FET device. The device architecture relies on a vertical gradient of functionality within the CEEL film. This configuration is illustrated in Fig. 2A, where gold microelectrodes serve as source and drain contacts, placed directly on top of the GO CEEL surface, and the HOPG substrate is employed as the back-gate electrode (see also Fig. S11B). As grown, the GO film is insulating. To define the FET active channel, we apply a preconditioning voltage (gate bias of +2.5 V and source-drain of 1 V) for 3 min. This initiates a positive feedback loop in which localized Joule heating thermally reduces the GO film's top surface. As more current flows, the heat generated increases, establishing a conductive path between the source and drain contacts. Crucially, the deeper layers of the film, which are in thermal contact with the bulk graphite heat sink, remain oxidized and insulating. These bottom layers function as the gate dielectric, effectively isolating the channel from the HOPG back-gate. This results in a monolithic gate (HOPG)/dielectric (bulk GO)/channel (surface rGO) stack, all made from the same carbon substrate.

Further details on characterization and the preconditioning step are provided in the Supporting Information, paragraph “Transistor characterization” (Fig. S14). The output characteristics in Fig. 2B show excellent linearity of I_D vs V_{DS} across different negative gate voltages, suggesting a low barrier to hole injection. As the gate voltage becomes more negative, the hole concentration (the majority charge carriers in GO) increases, attracting holes to the channel and thereby increasing I_D. The transfer characteristics I_D-V_{GS} plot in Fig. 2C exhibits V-shaped ambipolar behavior, with the Dirac point at a positive gate voltage (+0.148 V). This positive shift in the charge neutrality point confirms p-type doping of the GO channel, consistent with the electron-withdrawing nature of the remaining oxygen-containing groups, as reported in previous studies [49]. The inset in Fig. 2C shows the current modulation across the channel, with consistent switching between ON and OFF states under gate voltage, further confirming its function as an FET. These results provide a striking demonstration of CEEL's potential for straightforward fabrication of all-carbon electronics.

In addition to GO reduction via electrical currents, CEEL enables the development of more complex structures by combining with laser writing, as schematically illustrated in Fig. 2D. For this, we utilized a computer-controlled laser-scanning platform equipped with a 532 nm laser, focused through a 100x objective onto the sample. This process defines the “Rewrite” step in our workflow, in which the GO film can be selectively reverted to a graphene-like structure, namely LrGO. This process enables the formation of free-form electrically conductive structures, as demonstrated by AFM topography (Fig. 2E), surface potential (Fig. 2F), and local conductivity measurements of the same LrGO butterfly pattern (Fig. 2G). The LrGO butterfly appears as an engraved depression in the image topography in Fig. 2E due to the reduction in volume of the GO film layer resulting from the removal of oxygen-containing groups [48]. The Kelvin probe force microscopy image in Fig. 2F shows a well-defined contrast between the butterfly pattern and the surrounding GO, indicating a lower LrGO work function. The low surface potential of the GO film (i.e., a high work function) is attributable to the electron-withdrawing nature of the oxygen-containing

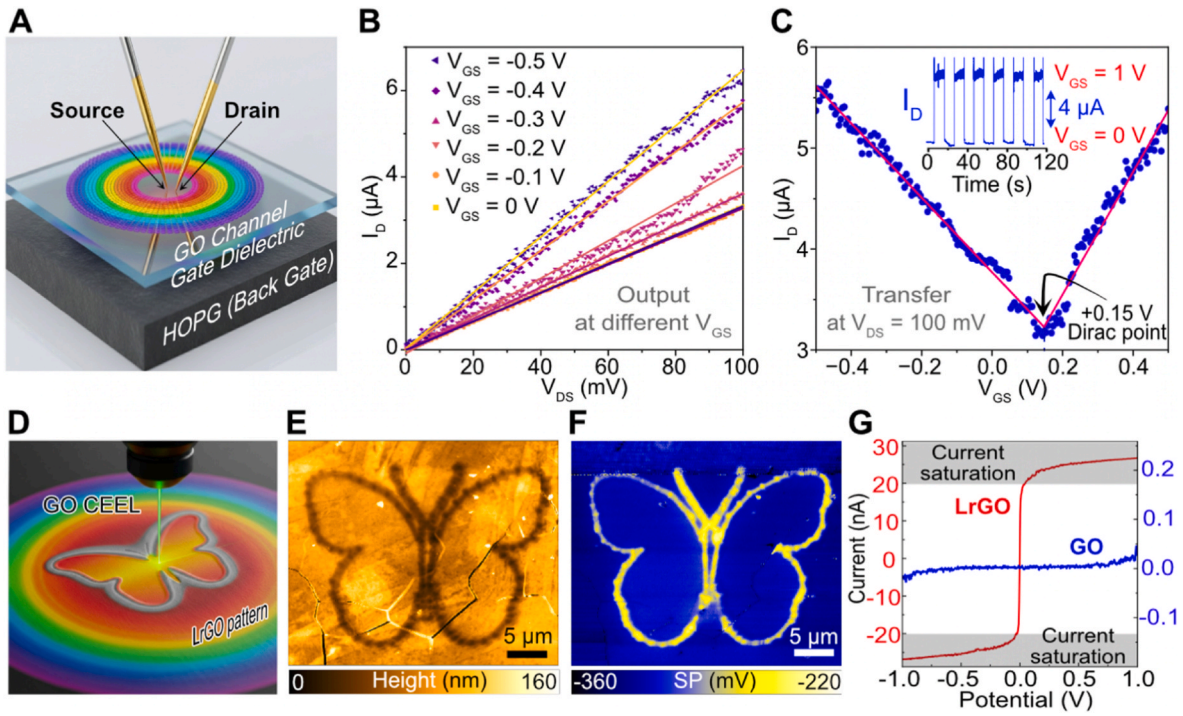

Fig. 2. (A) Schematic of the all-carbon, back-gated FET architecture. Two microprobes (Source and Drain) are placed on the in situ-grown GO film, which serves as the channel and gate dielectric, with the underlying HOPG serving as the back gate. (B) Output characteristics (I_D vs. V_{DS}) of the FET at various fixed gate-source voltages (V_{GS}), demonstrating precise gate modulation of the channel conductance. (C) Transfer characteristics (I_D vs. V_{GS}) showing p-type doping ambipolar behavior. The inset shows repeatable switching between high- and low-conductance states. (D) Schematic of the laser "Rewrite" process, creating an LrGO pattern. (E) AFM topography of a laser-written LrGO butterfly. (F) Corresponding Kelvin probe force microscopy map showing a significant drop in work function in the LrGO pattern. (G) Conductive-AFM I–V curves confirming the insulating nature of GO and the conductive nature of LrGO butterfly. The gray rectangles show the current saturation of our instrumentation.

groups [49]. The laser rewrite process removes oxygen-containing groups, thereby restoring the sp^2 carbon character of the original graphite substrate and lowering the work function [22]. Moreover, I–V curves in Fig. 2G locally recorded at the butterfly and at the GO nearby show drastic differences in electrical conductivity, transforming GO from an insulator to an Ohmic-like LrGO conductor. This capability to spatially control electronic properties is critical for engineering Schottky junctions, diodes, and FET channels and contacts.

The nature of the chemical changes during our Write-Rewrite steps was investigated using XPS. At each modification step, from bare HOPG to LrGO, we measured survey spectra and high-definition spectra from the C1s and O1s regions to track the chemical changes introduced. We defined the figure of merit for chemical changes in our workflow as the sp^2/sp^3 ratio, an indicator of the reduction-oxidation state of carbon species [50]. This figure of merit was calculated as the ratio between peak areas attributed to the respective component in the C1s high-definition spectra from HOPG, GO, and LrGO (Fig. 3A–C). For GO, this ratio is approximately 0.24, whereas the Rewrite step, following laser treatment, significantly increased the sp^2/sp^3 ratio to approximately 1.92. Comparing the obtained results with the XPS data provided by one of the largest worldwide suppliers of GO (Graphenea, Spain), we observed that the oxygen content is lower in our case (~27 % vs. 41–50 % for GO obtained using the modified Hummers' method). Another observation is that the XPS spectra provided by Graphenea mostly show C–O–C groups, with a small amount of C–O and C═O. In contrast, the GO obtained by CEEL contains significant amounts of C–O and C═O groups, which attach to the basal graphene plane and edges, respectively, suggesting a uniform distribution of oxygen-containing groups [51]. This uniform distribution between edge and basal-plane sites is consistent with our interpretation that MoS_2 activates ROS that attack the less reactive basal plane of graphene. The survey and O1s high-definition spectra for all samples (Fig. S15), along with a description of all spectra obtained, are presented in the Supporting Information.

This surface chemical analysis reveals that CEEL enables successful oxidation of the HOPG surface by introducing oxygen-containing groups, similar to those found in conventional GO obtained by the modified Hummers' method [52]. Similar to conventional GO, GO CEEL can be laser-reduced to partially restore the initial conjugated sp^2 carbon network.

These observations were complemented by SEM and EDX, which provided better spatial resolution than XPS but were limited to elemental information and less surface-sensitive, with a larger information depth of a few hundred nanometers. Fig. 3D shows a low-magnification SEM image of the CEEL pattern delineated by the dotted green line. The high-magnification SEM image in Fig. 3E shows the region where the Rewrite process occurred, with a grid and butterflies drawn on the GO canvas, confirming the process's precision and high resolution. On both SEM images, we marked by numbers some representative locations, varying from outside of the CEEL pattern (location 1) towards the center (locations 2–4) and the LrGO butterfly (location 5) created during Rewrite. The EDX spectra from these locations are shown in Fig. 3F, demonstrating a monotonic decrease in oxygen relative to carbon as we approach the center of the pattern (locations 1–4). This spatially resolved elemental analysis reveals that CEEL induces carbon oxidation that radially follows the electric field, whereas the Rewrite process locally reduces the oxygen content from 17 % to 3.2 % (atomic percentage) by releasing oxygen-containing groups (Fig. S16).

LrGO surface, decorated with metallic nanostructures, is a promising platform for photocatalytic and sensing applications. Gold and silver nanostructures are widely used as photocatalytic and plasmonic materials, allowing effective conversion of various chemicals [53,54]. Another potential application implies the use of metallic nanostructures

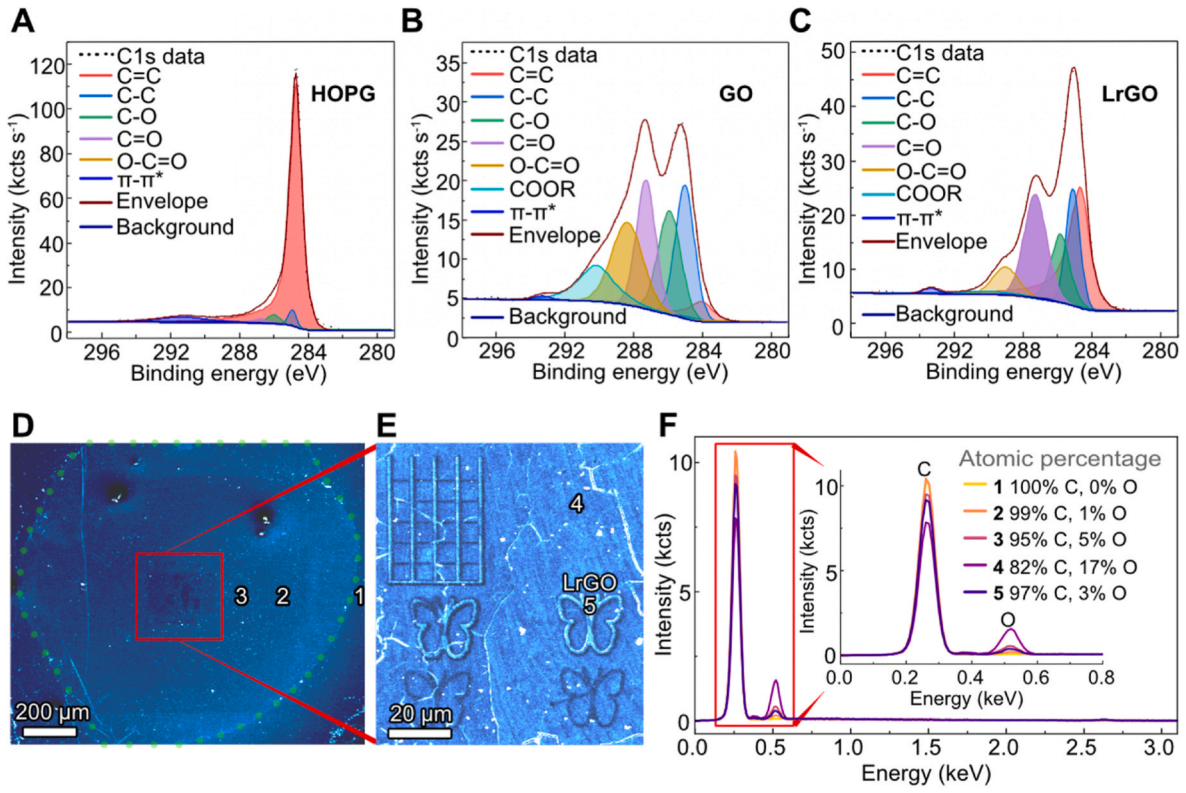

Fig. 3. (A–C) High-resolution C1s XPS spectra of pristine HOPG, in-situ grown GO, and LrGO, respectively. The spectra show the initial sp^2 C–C bonds of HOPG, the emergence of C–O bonds upon electrochemical oxidation to GO, and the subsequent removal of these oxygen groups upon laser reduction to LrGO. (D) SEM image of a GO surface with multiple laser-written patterns. (E) A magnified view of the patterns from the region marked '4′ in (D). (F) Spatially resolved EDX spectra taken from different locations on the surface shown in (D) and (E). The inset quantifies the atomic percentage of carbon and oxygen, showing a clear, localized decrease in oxygen content within the LrGO patterns compared to the surrounding GO.

as a sensing platform for biomedical applications. For instance, it can be functionalized with specific ligands to tailor nanostructure properties and enhance its effectiveness for biomolecule detection and disease diagnosis [55,56]. Additional investigation of the added functionality was performed by rewriting LrGO microelectrodes on a GO pattern and using them to electrochemically reduce gold Au^{3+} ions, as illustrated in Fig. 4A. This process, the "Direct" step in our workflow, enables the on-demand creation of Au nanostructures selectively on a LrGO grid, demonstrating that the rewriting process produces structures conductive enough to support spatially-resolved electrochemical reactions. This idea was verified by EDX analysis, which showed selective gold deposition on the LrGO grid pattern, as evidenced by the spectra in Fig. 4B. The insets in Fig. 4B correspond to optical microscopy images before and after Au deposition, as indicated by the yellow hollow characteristic of gold. This observation was confirmed by SEM imaging of a grid corner (Fig. 4C), which revealed the formation of Au clusters.

We demonstrated the generality of our approach by fabricating additional metal nanostructures, including Ag. The selective deposition of Ag nanostructures enables the creation of patterns with dual functionality: plasmonic nanoantennas that amplify the Raman signal of the molecule via SERS and photocatalytic reactors that generate plasmons that decay into hot electrons and heat, thereby converting 4-NBT into DMAB. For this reaction, another method for surface characterization is XPS. However, the N1s signal of 4-NBT and DMAB in XPS is weak, peak deconvolution is challenging, and no significant spectral changes are observed—unlike in Raman spectroscopy, where the nitro ($–NO_2$) and azo (–N═N–) functional groups, characteristic of 4-NBT and DMAB, respectively, are unambiguously identifiable [57]. This enhanced detection is enabled by SERS, which significantly amplifies the vibrational signatures of molecules adsorbed on plasmonically active surfaces. In study [57], the authors investigated the photocatalytic conversion of 4-NBT to DMAB using both XPS and Raman spectroscopy and concluded that Raman spectroscopy is more powerful than XPS for this conversion. The photocatalytic conversion of 4-NBT to DMAB was confirmed by hyperspectral Raman imaging, as shown in Fig. 4D, where red-color-coded regions indicate the presence of the DMAB photocatalytic product overlapping the grid where Ag nanostructures were selectively grown. The elegance of this approach lies in our ability to monitor the photocatalytic reaction in real time, enabled by the built-in SERS sensing capabilities of the plasmonic Ag nanostructures. This analysis revealed that while 4-NBT is present around the sample (black particles in Fig. S17), photocatalytic conversion to DMAB occurs only in the laser-rewritten grid as we see the appearance of the characteristic azo (–N═N–) functional groups in DMAB at 1437 cm^{-1} at spots 2 and 4 (see Fig. 4E), indicating the importance of laser processing in spatially defining photocatalytic reactions. These results demonstrate a method for applying CEEL to address a gap in graphene oxide photonics by integrating it with plasmonic systems [58].

4. Conclusion

In summary, we have established a complete "Write-Rewrite-Direct" platform for the sequential engineering of carbon's optical, electronic, and chemical properties.

This development pushes carbon electronics beyond traditional electrochemical or laser methods by introducing CEEL, which enables **monolithic integration without the need for material transfer, film deposition, or lift-off**.

The key novelty and impact points of this work are:

1) The epitaxy-like "Writing" of GO photonic structures with radially varying structural colors via thin-film interference generated by

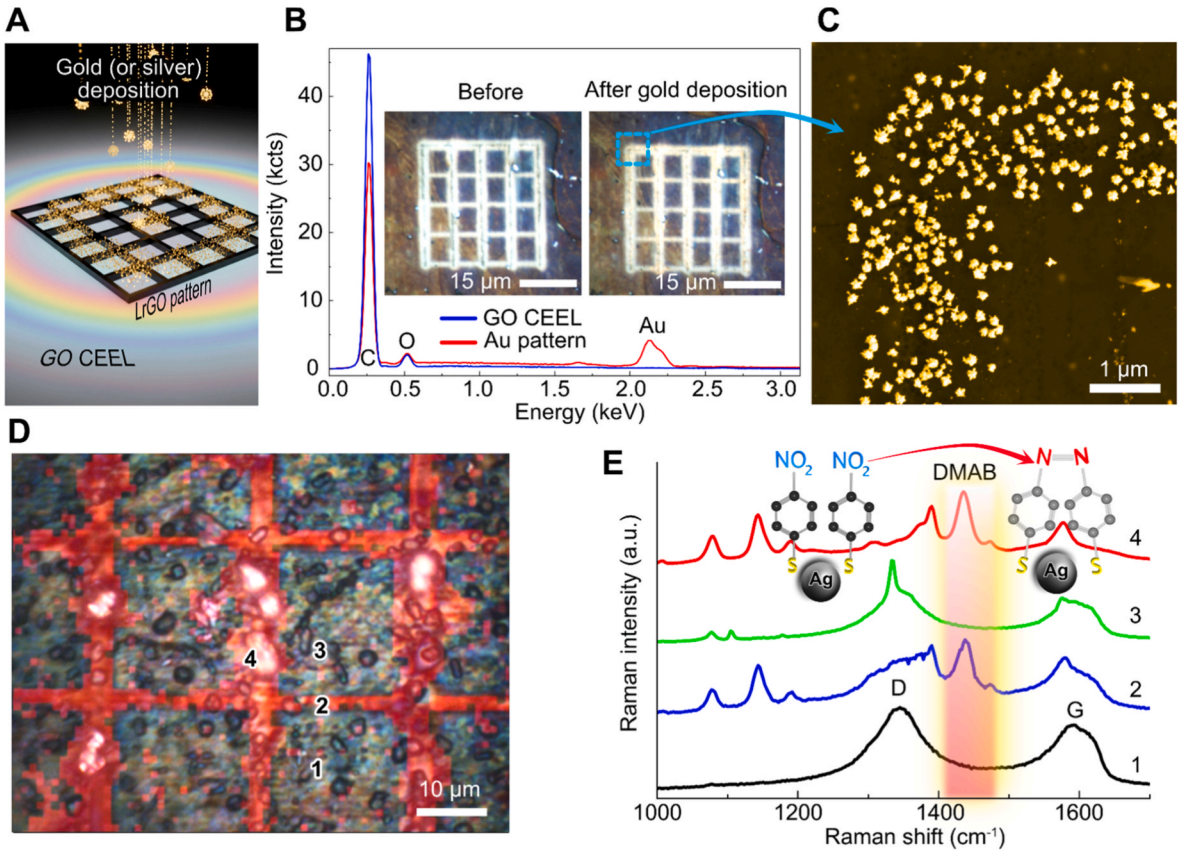

Fig. 4. (A) Schematic of the "Direct" process, where the LrGO pattern acts as a template for the selective electrochemical deposition of metal nanostructures. (B) EDX spectra comparing a region with gold deposited on LrGO to an adjacent GO region, confirming the high selectivity of the deposition. Insets show corresponding optical micrographs of a pattern before and after gold deposition. (C) High-magnification SEM image revealing the 3D, star-like morphology of the electrodeposited gold nanoclusters. (D) Combined optical micrograph and SERS map of an LrGO grid functionalized with silver (Ag) nanoparticles. The red overlay shows the selective presence of the DMAB Raman peak, confirming that the photocatalytic reaction is localized exclusively to the Ag-decorated LrGO pattern. (E) In-situ SERS spectra taken from different locations of the sample (marked in Fig. 4d). The Ag-decorated LrGO grid (spectra 2 and 4) shows the laser-induced photocatalytic conversion of 4-NBT (spectrum 4) to DMAB over time. Spectrum 1 obtained outside the grid shows no 4-NBT or DMAB signals, but the typical carbon peaks from GO dominate the spectrum. (For interpretation of the references to color in this figure legend, the reader is referred to the Web version of this article.)

leveraging the electrocatalytic properties of MoS_2 to enhance water splitting. The MoS_2 catalytic effect enables the fabrication of **smooth, long-lasting GO surfaces with the most intense colors reported to date for GO films** (Fig. S11) . Moreover, these structures have superior mechanical robustness compared to conventional GO-based films. The remarkable optical response to environmental changes enables low-cost, smart carbon surfaces and sensors.

2) Unlike GO produced through chemical oxidation (Hummers' method), our process has a lower environmental impact and generates no waste. In contrast to most electrochemical methods that rely on concentrated sulfuric acid, **our acid-free, ambient-temperature approach is eco-friendly and easy to use.**
3) The materials we obtain enable applications from optical sensors to active electronics. We exploited the intrinsic vertical structure of the GO CEEL on HOPG to create the **first monolithic all-carbon back-gated FET**, exhibiting clear and switchable p-type output characteristics without the need for transfer or deposition.

This GO CEEL film works as a canvas to “Rewrite” free-form electrically conductive structures with a spatial resolution limited by the diffraction limit of light (~λ/2). The “Direct” step was demonstrated by the selective deposition of gold- or silver-based metallic nanostructures, creating a plasmonic microreactor capable of inducing and detecting photocatalytic reactions in real time via SERS.

Although we focused here on programming the electronic and chemical properties of GO CEEL structures, follow-up work could exploit their intrinsic gradient-index optical properties to create all-carbon optical elements, including spectral filters and planar lenses. In conclusion, we have engineered one of the oldest known materials, creating multifunctional smart surfaces for monolithic all-carbon electronics and sensing applications.

CRediT authorship contribution statement

Raul D. Rodriguez: Writing – review & editing, Writing – original draft, Visualization, Validation, Supervision, Project administration, Methodology, Investigation, Funding acquisition, Formal analysis, Data curation, Conceptualization. **Pavel Bakholdin:** Writing – review & editing, Writing – original draft, Visualization, Investigation, Formal analysis, Data curation. **Tuan-Hoang Tran:** Writing – review & editing, Writing – original draft, Visualization, Methodology, Investigation, Formal analysis, Data curation. **Elizaveta Dogadina:** Writing – review & editing, Writing – original draft, Visualization, Investigation, Formal analysis, Data curation. **Dmitry Cheshev:** Writing – review & editing, Investigation, Data curation. **Dmitry Kogolev:** Formal analysis, Data curation. **Maxim Fatkullin:** Writing – review & editing, Investigation, Formal analysis, Data curation. **Jin-Ju Chen:** Writing – review & editing. **Tian Ma:** Writing – review & editing. **Shuang Li:** Writing – review & editing. **Chong Cheng:** Writing – review & editing. **Evgeniya Sheremet:** Writing – review & editing, Formal analysis.

Declaration of competing interest

The authors declare that they have no known competing financial interests or personal relationships that could have appeared to influence the work reported in this paper.

Acknowledgements

The work was supported by the TPU development program Priority 2030. The authors thank Dr. K. Krukovskiy for the SEM/EDX measurements at the Center for Collective Use of the Institute of Strength Physics and Materials Science SB RAS "NANOTECH". The authors are grateful to the Center of TPU's “Physical and chemical methods of analysis” for the XPS measurements and to Prof. Pavel S. Postnikov for access to the XPS facility.

Appendix B. Supplementary data

Supplementary data to this article can be found online at https://doi.org/10.1016/j.carbon.2025.121215.

References

[1] H. Amani, H. Arzaghi, M. Bayandori, A.S. Dezfuli, H. Pazoki-Toroudi, A. Shafiee, L. Moradi, Controlling cell behavior through the design of biomaterial surfaces: a focus on surface modification techniques, Adv. Mater. Interfaces 6 (2019) 1900572, https://doi.org/10.1002/admi.201900572.

[2] S. Çelen, H. Özden, Laser-induced novel patterns: as smart strain actuators for new-age dental implant surfaces, Appl. Surf. Sci. 263 (2012) 579–585, https://doi.org/10.1016/j.apsusc.2012.09.112.

[3] T.-H. Tran, R.D. Rodriguez, N.E. Villa, S. Shchadenko, A. Averkiev, Y. Hou, T. Zhang, A. Matkovic, E. Sheremet, Laser-induced photothermal activation of multilayer MoS_2 with spatially controlled catalytic activity, J. Colloid Interface Sci. 654 (2024) 114–123, https://doi.org/10.1016/j.jcis.2023.10.027.

[4] A. Lipovka, M. Fatkullin, S. Shchadenko, I. Petrov, A. Chernova, E. Plotnikov, V. Menzelintsev, S. Li, L. Qiu, C. Cheng, R.D. Rodriguez, E. Sheremet, Textile electronics with laser-induced graphene/polymer hybrid fibers, ACS Appl. Mater. Interfaces 15 (2023) 38946–38955, https://doi.org/10.1021/acsami.3c06968.

[5] R.D. Rodriguez, M. Fatkullin, A. Garcia, I. Petrov, A. Averkiev, A. Lipovka, L. Lu, S. Shchadenko, R. Wang, J. Sun, Q. Li, X. Jia, C. Cheng, O. Kanoun, E. Sheremet, Laser-engineered multifunctional graphene-glass electronics, Adv. Mater. 34 (2022) 2206877, https://doi.org/10.1002/adma.202206877.

[6] Y.C. Guan, Y.W. Fang, G.C. Lim, H.Y. Zheng, M.H. Hong, Fabrication of laser-reduced graphene oxide in liquid nitrogen environment, Sci. Rep. 6 (2016) 28913, https://doi.org/10.1038/srep28913.

[7] A.A. Faqihi, N. Keegan, L. Šiller, J. Hedley, Effect of ambient environment on laser reduction of graphene oxide for applications in electrochemical sensing, Sensors 23 (2023) 8002, https://doi.org/10.3390/s23188002.

[8] S.W. Lee, C. Mattevi, M. Chhowalla, R. Mohan Sankaran, Plasma-assisted reduction of graphene oxide at low temperature and atmospheric pressure for flexible conductor applications, J. Phys. Chem. Lett. 3 (2012) 772–777, https://doi.org/10.1021/jz300080p.

[9] W. Li, M. Wojcik, K. Xu, Optical microscopy unveils rapid, reversible electrochemical oxidation and reduction of graphene, Nano Lett. 19 (2019) 983–989, https://doi.org/10.1021/acs.nanolett.8b04216.

[10] T. Chen, Y. Zhang, W. Xu, Observing the heterogeneous electro-redox of individual single-layer graphene sheets, ACS Nano 10 (2016) 8434–8442, https://doi.org/10.1021/acsnano.6b03327.

[11] O.Ö. Ekiz, M. Ürel, H. Güner, A.K. Mizrak, A. Dâna, Reversible electrical reduction and oxidation of graphene oxide, ACS Nano 5 (2011) 2475–2482, https://doi.org/10.1021/nn1014215.

[12] M. Fatkullin, I. Petrov, E. Dogadina, D. Kogolev, A. Vorobiev, P. Postnikov, J.-J. Chen, R.F. de Oliveira, O. Kanoun, R.D. Rodriguez, E. Sheremet, Electrochemical switching of laser-induced graphene/polymer composites for tunable electronics, Polymers 17 (2025) 192, https://doi.org/10.3390/polym17020192.

[13] D.B. Farmer, R. Golizadeh-Mojarad, V. Perebeinos, Y.-M. Lin, G.S. Tulevski, J. C. Tsang, P. Avouris, Chemical doping and electron-hole conduction asymmetry in graphene devices, Nano Lett. 9 (2009) 388–392, https://doi.org/10.1021/nl803214a.

[14] R.D. Rodriguez, A. Khalelov, P.S. Postnikov, A. Lipovka, E. Dorozhko, I. Amin, G. V. Murastov, J.-J. Chen, W. Sheng, M.E. Trusova, M.M. Chehimi, E. Sheremet, Beyond graphene oxide: laser engineering functionalized graphene for flexible electronics, Mater. Horiz. 7 (2020) 1030–1041, https://doi.org/10.1039/C9MH01950B.

[15] E. Dogadina, R.D. Rodriguez, M. Fatkullin, A. Lipovka, A. Kozelskaya, A. Averkiev, E. Plotnikov, X. Jia, C. Liu, J.-J. Chen, C. Cheng, L. Qiu, S. Tverdokhlebov, E. Sheremet, Integration of graphene into calcium phosphate coating for implant electronics, ACS Appl. Mater. Interfaces 17 (2025) 13527–13537, https://doi.org/10.1021/acsami.4c21046.

[16] A. Lipovka, I. Petrov, M. Fatkullin, G. Murastov, A. Ivanov, N.E. Villa, S. Shchadenko, A. Averkiev, A. Chernova, F. Gubarev, M. Saqib, W. Sheng, J.-J. Chen, O. Kanoun, I. Amin, R.D. Rodriguez, E. Sheremet, Photoinduced flexible graphene/polymer nanocomposites: design, formation mechanism, and properties engineering, Carbon 194 (2022) 154–161, https://doi.org/10.1016/j.carbon.2022.03.039.

[17] R.W. Murray, Nanoelectrochemistry: metal nanoparticles, nanoelectrodes, and nanopores, Chem. Rev. 108 (2008) 2688–2720, https://doi.org/10.1021/cr068077e.

[18] X. You, S. Maharjan, K. Vinodgopal, J.M. Atkin, Nanoscale insights into graphene oxide reduction by tip-enhanced Raman spectroscopy, Phys. Chem. Chem. Phys. 26 (2024) 9871–9879, https://doi.org/10.1039/D3CP04711C.

[19] M. Nose, T. Kinumoto, H.-S. Choo, K. Miyazaki, T. Abe, Z. Ogumi, Electrochemical oxidation of highly oriented pyrolytic graphite in sulphuric acid solution under potential pulse condition, Fuel Cells 9 (2009) 284–290, https://doi.org/10.1002/fuce.200800077.

[20] K.J. Aoki, H. Wang, J. Chen, T. Nishiumi, Formation of graphite oxide nano-disks by electrochemical oxidation of HOPG, Electrochim. Acta 130 (2014) 381–386, https://doi.org/10.1016/j.electacta.2014.03.044.

[21] H.-S. Choo, T. Kinumoto, M. Nose, K. Miyazaki, T. Abe, Z. Ogumi, Electrochemical oxidation of highly oriented pyrolytic graphite during potential cycling in sulfuric acid solution, J. Power Sources 185 (2008) 740–746, https://doi.org/10.1016/j.jpowsour.2008.07.086.

[22] M. Fatkullin, D. Cheshev, A. Averkiev, A. Gorbunova, G. Murastov, J. Liu, P. Postnikov, C. Cheng, R.D. Rodriguez, E. Sheremet, Photochemistry dominates over photothermal effects in the laser-induced reduction of graphene oxide by visible light, Nat. Commun. 15 (2024) 9711, https://doi.org/10.1038/s41467-024-53503-y.

[23] Y. Zhang, L. Guo, S. Wei, Y. He, H. Xia, Q. Chen, H.-B. Sun, F.-S. Xiao, Direct imprinting of microcircuits on graphene oxides film by femtosecond laser reduction, Nano Today 5 (2010) 15–20, https://doi.org/10.1016/j.nantod.2009.12.009.

[24] D.A. Sokolov, K.R. Shepperd, T.M. Orlando, Formation of graphene features from direct laser-induced reduction of graphite oxide, J. Phys. Chem. Lett. 1 (2010) 2633–2636, https://doi.org/10.1021/jz100790y.

[25] L. Tong, W. Qi, M. Wang, R. Huang, R. Su, Z. He, Tunable design of structural colors produced by pseudo-1D photonic crystals of graphene oxide, Small 12 (2016) 3433–3443, https://doi.org/10.1002/smll.201600148.

[26] U. Hofmann, W. Rüdorff, The formation of salts from graphite by strong acids, Trans. Faraday Soc. 34 (1938) 1017–1021, https://doi.org/10.1039/tf9383401017.

[27] A.A. Gewirth, A.J. Bard, In situ scanning tunneling microscopy of the anodic oxidation of highly oriented pyrolytic graphite surfaces, J. Phys. Chem. 92 (1988) 5563–5566, https://doi.org/10.1021/j100331a006.

[28] K. Luo, Y. Li, T. Liu, X. Zhuge, E. Chung, A.R. Timms, S.P. Graham, G. Ren, Functionalized copper nanoparticles with gold nanoclusters: part I. Highly selective electrosynthesis of hydrogen peroxide, ACS Omega 8 (2023) 36171–36178, https://doi.org/10.1021/acsomega.3c03665.

[29] Q. Li, B. Hu, Q. Yang, X. Cai, M. Nie, Y. Jin, L. Zhou, Y. Xu, Q. Pan, L. Fang, Interaction mechanism between multi-layered MoS_2 and H2O2 for self-generation of reactive oxygen species, Environ. Res. 191 (2020) 110227, https://doi.org/10.1016/j.envres.2020.110227.

[30] S. Pei, Q. Wei, K. Huang, H.-M. Cheng, W. Ren, Green synthesis of graphene oxide by seconds timescale water electrolytic oxidation, Nat. Commun. 9 (2018) 145, https://doi.org/10.1038/s41467-017-02479-z.

[31] T. Manyepedza, J.M. Courtney, A. Snowden, C.R. Jones, N.V. Rees, Impact electrochemistry of MoS_2: electrocatalysis and hydrogen generation at low overpotentials, J. Phys. Chem. C 126 (2022) 17942–17951, https://doi.org/10.1021/acs.jpcc.2c06055.

[32] A.Y.S. Eng, A. Ambrosi, C.K. Chua, F. Sanĕk, Z. Sofer, M. Pumera, Unusual inherent electrochemistry of graphene oxides prepared using permanganate oxidants, Chem. Eur J. 19 (2013) 12673–12683, https://doi.org/10.1002/chem.201301889.

[33] L. Dong, Z. Chen, S. Lin, K. Wang, C. Ma, H. Lu, Reactivity-controlled preparation of ultralarge graphene oxide by chemical expansion of graphite, Chem. Mater. 29 (2017) 564–572, https://doi.org/10.1021/acs.chemmater.6b03748.

[34] P. Zhang, P. He, Y. Zhao, S. Yang, Q. Yu, X. Xie, G. Ding, Oxidating fresh porous graphene networks toward ultra-large graphene oxide with electrical conductivity, Adv. Funct. Mater. 32 (2022) 2202697, https://doi.org/10.1002/adfm.202202697.

[35] J. Shang, L. Ma, J. Li, W. Ai, T. Yu, G.G. Gurzadyan, The origin of fluorescence from graphene oxide, Sci. Rep. 2 (2012) 792, https://doi.org/10.1038/srep00792.

[36] P. Chen, B. Liu, L. Chen, W. Wang, P. Zhang, Y. Cui, L. Ruan, X. Chang, The structural origin of photoluminescence in graphene oxide revealed by 13C stable isotopic labeling, Carbon 244 (2025) 120734, https://doi.org/10.1016/j.carbon.2025.120734.

[37] J. Zhu, C.M. Andres, J. Xu, A. Ramamoorthy, T. Tsotsis, N.A. Kotov, Pseudonegative thermal expansion and the state of water in graphene oxide layered assemblies, ACS Nano 6 (2012) 8357–8365, https://doi.org/10.1021/nn3031244.

[38] N. Chandrasekar, R. Balaji, R.S. Perala, N.Z. Nik Humaidi, K. Shanmugam, Y.-C. Liao, M.T. Hwang, S. Govindaraju, A brief review of graphene-based biosensors developed for rapid detection of COVID-19 biomarkers, Biosensors 13 (2023) 307, https://doi.org/10.3390/bios13030307.

[39] D. Lutomia, R. Poria, D. Kala, A.K. Singh, M.K. Gupta, D. Kumar, A. Kaushal, S. Gupta, Unlocking the potential of 2D nanomaterial-based biosensors in

biomarker-based detection of Helicobacter pylori, Mater. Adv. 6 (2025) 117–142, https://doi.org/10.1039/D4MA00546E.
[40] Y. Xie, D. Zhao, 2D materials: a wonderland for physical science, Natl. Sci. Rev. 9 (2022), https://doi.org/10.1093/nsr/nwab202.
[41] D.V. Andreeva, K.S. Novoselov, Multifunctional 2D materials for antiviral protection and detection, Natl. Sci. Rev. 9 (2022), https://doi.org/10.1093/nsr/nwab095.
[42] Chronic obstructive pulmonary disease (COPD), (n.d.). https://www.who.int/news-room/fact-sheets/detail/chronic-obstructive-pulmonary-disease-(copd) (accessed September 18, 2025).
[43] I. Jung, J.-S. Rhyee, J.Y. Son, R.S. Ruoff, K.-Y. Rhee, Colors of graphene and graphene-oxide multilayers on various substrates, Nanotechnology 23 (2011) 025708, https://doi.org/10.1088/0957-4484/23/2/025708.
[44] N. Cao, Y. Zhang, Study of reduced graphene oxide preparation by Hummers' method and related characterization, J. Nanomater. 2015 (2015) 168125, https://doi.org/10.1155/2015/168125.
[45] W.S. Hummers Jr., R.E. Offeman, Preparation of graphitic oxide, J. Am. Chem. Soc. 80 (1958) 1339, https://doi.org/10.1021/ja01539a017.
[46] M. Zhan, M. Xu, W. Lin, H. He, C. He, Graphene oxide research: current developments and future directions, Nanomaterials 15 (2025) 507, https://doi.org/10.3390/nano15070507.
[47] J. Henrie, S. Kellis, S. Schultz, A. Hawkins, Electronic color charts for dielectric films on silicon, Opt. Express 12 (2004) 1464–1469, https://doi.org/10.1364/OPEX.12.001464.
[48] G.V. Murastov, A.A. Lipovka, M.I. Fatkullin, R.D. Rodriguez, E.S. Sheremet, Laser reduction of graphene oxide: local control of material properties, Phys. Usp. 66 (2023) 1105–1113, https://doi.org/10.3367/UFNe.2022.12.039291.
[49] L. Sygellou, G. Paterakis, C. Galiotis, D. Tasis, Work function tuning of reduced graphene oxide thin films, J. Phys. Chem. C 120 (2016) 281–290, https://doi.org/10.1021/acs.jpcc.5b09234.
[50] D.W. Lee, J.W. Seo, sp^2/sp^3 carbon ratio in graphite oxide with different preparation times, J. Phys. Chem. C 115 (2011) 2705–2708, https://doi.org/10.1021/jp107906u.
[51] Graphene Oxide Water Dispersion (0.4 wt% concentration), Graphenea (n.d.). https://www.graphenea.com/products/graphene-oxide-4-mg-ml-water-dispersion-1000-ml (accessed September 17, 2025).
[52] J. Guerrero-Contreras, F. Caballero-Briones, Graphene oxide powders with different oxidation degree, prepared by synthesis variations of the hummers method, Mater. Chem. Phys. 153 (2015) 209–220, https://doi.org/10.1016/j.matchemphys.2015.01.005.
[53] D. Cheng, R. Liu, K. Hu, Gold nanoclusters: photophysical properties and photocatalytic applications, Front. Chem. 10 (2022) 958626, https://doi.org/10.3389/fchem.2022.958626.
[54] R. Sharma, R. Bharti, A review on the synthesis and Photocatalytic application of silver nano particles, IOP Conf. Ser. Earth Environ. Sci. 1110 (2023) 012021, https://doi.org/10.1088/1755-1315/1110/1/012021.
[55] Y. Chen, Y. Xianyu, X. Jiang, Surface modification of gold nanoparticles with small molecules for biochemical analysis, Acc. Chem. Res. 50 (2017) 310–319, https://doi.org/10.1021/acs.accounts.6b00506.
[56] A.J. Mieszawska, W.J.M. Mulder, Z.A. Fayad, D.P. Cormode, Multifunctional gold nanoparticles for diagnosis and therapy of disease, Mol. Pharm. 10 (2013) 831–847, https://doi.org/10.1021/mp3005885.
[57] L. Yang, C. Zhao, J. Xu, J. Guo, Z. Gao, Y.-Y. Song, Boosting the Raman signal on a semiconductornanotube membrane for reporting photocatalytic reactions on site, Chem. Commun. 56 (2020) 10333–10336, https://doi.org/10.1039/D0CC04396F.
[58] J. Wu, H. Lin, D.J. Moss, K.P. Loh, B. Jia, Graphene oxide for photonics, electronics and optoelectronics, Nat. Rev. Chem 7 (2023) 162–183, https://doi.org/10.1038/s41570-022-00458-7.